

# Magnetically tunable random lasing in polymer-dispersed chiral liquid crystals: Experimental and machine learning insights

Cite as: J. Appl. Phys. 138, 213104 (2025); doi: 10.1063/5.0303645

Submitted: 23 September 2025 · Accepted: 16 November 2025 ·

Published Online: 1 December 2025



View Online



Export Citation



CrossMark

Aneela Ahmad,<sup>1</sup> Haitao Dai,<sup>1,2,a)</sup> Rafiul Haq,<sup>3</sup> Shouzhong Feng,<sup>4</sup> Aisha Rani,<sup>5</sup> Buyi Yao,<sup>1</sup> and Yuhan Wang<sup>1</sup>

## AFFILIATIONS

<sup>1</sup>Tianjin Key Laboratory of Low Dimensional Materials Physics and Preparing Technology, School of Science, Tianjin University, Tianjin 300072, China

<sup>2</sup>The International Joint Institute of Tianjin University, Fuzhou, Tianjin University, Tianjin 300072, China

<sup>3</sup>College of Intelligence and Computing, Tianjin University, Tianjin 300350, China

<sup>4</sup>Anhui Zhongyi New Materials Technology Co., Ltd., Chuzhou 239599, Anhui, China

<sup>5</sup>School of Environmental Science & Engineering, Tianjin University, Tianjin 300350, People's Republic of China

<sup>a)</sup>Author to whom correspondence should be addressed: [daihaitao@tju.edu.cn](mailto:daihaitao@tju.edu.cn)

06 December 2025 08:36:25

## ABSTRACT

This work investigates magnetically tunable random lasing in polymer-dispersed chiral liquid crystals (PDCLCs) doped with ferromagnetic nanoparticles (MNPs) in a capillary system. The alignment of liquid crystal molecules, modulated by external magnetic fields, strongly influences the lasing dynamics. We systematically studied the effects of MNP concentration and the amplitude and orientation of the magnetic field on key emission characteristics, including the lasing threshold, the spectral envelope, and intensity. To model these nonlinear interactions and permit prediction, supervised regression models were trained using experimental data. Four machine-learning algorithms (random forest, support vector machines, artificial neural networks, and XGBoost) were tested, and the XGBoost model yielded the best results ( $R^2 = 0.9752$ ) on the test set. Importance analysis revealed that magnetic-field strength and MNP concentration are the dominant factors governing lasing behavior. The results highlight the intricate interplay between magnetic-field modulation and nanoparticle doping in PDCLC-based random lasers, underscoring the potential of machine learning in optimizing future optoelectronic and photonic devices.

© 2025 Author(s). All article content, except where otherwise noted, is licensed under a Creative Commons Attribution-NonCommercial 4.0 International (CC BY-NC) license (<https://creativecommons.org/licenses/by-nc/4.0/>). <https://doi.org/10.1063/5.0303645>

## I. INTRODUCTION

Random lasing is the generation of coherent light in a disordered gain medium in the absence of a conventional resonant cavity due to the effects of multiple scattering and optical amplification. This phenomenon has generated significant interest, as it is utilized in tunable lasers, optical sensors, and compact photonic devices.<sup>1</sup>

Cholesteric liquid crystals, also known as chiral nematic liquid crystals, are helical structures and exhibit a photonic bandgap, resulting in circularly selective reflection.<sup>2</sup> When filled with fluorescent dyes, they are capable of allowing mirror-free lasing within the stop band.<sup>3</sup> Recently, bio-based and sustainable approaches,

such as cellulose nanocrystal-derived chiral liquid crystal films, have also been explored for photonic and lasing applications.<sup>4</sup> In polymer-dispersed chiral liquid crystals (PDCLCs), the helical order (polymer-dispersed) exists simultaneously with the polymer domain (structural disorder). This combination achieves both feedback and scattering; thus, PDCLCs are a promising platform for random lasing. Magnetic-field control has been less explored, although previous studies have demonstrated that PDCLCs can be regulated by electric field, temperature, or mechanical means.<sup>5,6</sup> In addition, photo-switchable chiral dopants provide another effective route to dynamically construct and control liquid crystal helical structures under light stimuli.<sup>7</sup>

Doping PDCLCs with magnetic nanoparticles (MNPs), such as  $\text{Fe}_3\text{O}_4$ , offers a novel mechanism to tune random lasing behavior magnetically. Under an applied magnetic field, the induced alignment of liquid crystal molecules and MNPs modulates scattering pathways and feedback mechanisms, leading to shifts in emission intensity, threshold, and spectral features depending on MNP concentration and field orientation.<sup>8–10</sup> A foundational study by Dai *et al.* demonstrated magnetic field-controlled lasing in  $\text{Fe}_3\text{O}_4$  doped PDLCs within a capillary, showing a clear dependence of the threshold, spectral envelope, and intensity on both field strength and concentration.<sup>11</sup> Moreover, random lasing has also been realized in dye-doped chiral nematic liquid crystals, confirming their potential as versatile disordered lasing media.<sup>12</sup>

Despite these advances, the lasing dynamics in such systems remain highly nonlinear and multidimensional, influenced simultaneously by magnetic-field strength and direction, pump energy, and nanoparticle concentration. Conventional parametric approaches often struggle to capture these interdependences or provide predictive insights for unexplored conditions. Machine learning (ML) has recently emerged as a powerful tool for modeling complex physical systems in photonics and materials science.<sup>13</sup> Prior studies have shown that supervised learning models can predict random laser emission fluctuations from experimental observables, while more broadly, ML and deep learning approaches are being leveraged to design and optimize photonic devices, lasers, and sensors.<sup>14,15</sup>

In this study, we investigate the random lasing properties of polymer-dispersed cholesteric liquid crystal (PDCLC) samples doped with ferromagnetic metallic nanoparticles (MNPs) within capillaries. Experimental results reveal that the random lasing emission-intensity peaks at an MNP concentration of 0.02 wt. %, decreasing at higher concentrations due to excessive scattering. The random lasing spectrum undergoes a distinct blue shift in the center of the envelope as the concentration of MNP increases. Subjected to a parallel magnetic field ( $B_{||}$ ), the lasing intensity is significantly higher and displays a more pronounced blue shift compared to a transverse magnetic field ( $B_{\perp}$ ). However, stronger magnetic fields in both orientations tend to suppress lasing emission due to the alignment of liquid crystal molecules, which reduces scattering. To gain insight in these complicated relationships, we will use machine-learning models, such as Artificial Neural Networks (ANNs),<sup>16</sup> Support Vector Machines (SVMs),<sup>17</sup> Random Forest (RF),<sup>18</sup> and XGBoost,<sup>19</sup> to predict lasing intensity and discover the most important factors affecting the emission characteristics. Such models provide ways to observe the dynamics of nonlinearity in random lasing and optimize the PDCLC-based systems.

This research combines accurate experimental monitoring and data-driven modeling to provide insight into the interaction between nanoparticle doping and magnetic-field effects on random lasing. Our results pave the way for the next generation of tunable lasers and optoelectronic devices, with applications in sensing, imaging, and optical communication.

## II. METHODOLOGY

Figure 1 is a diagram of the pump light path used in the experiment. The pulsed laser output from the laser passes through a polarizing beam splitter (BS): one part is used as the pump

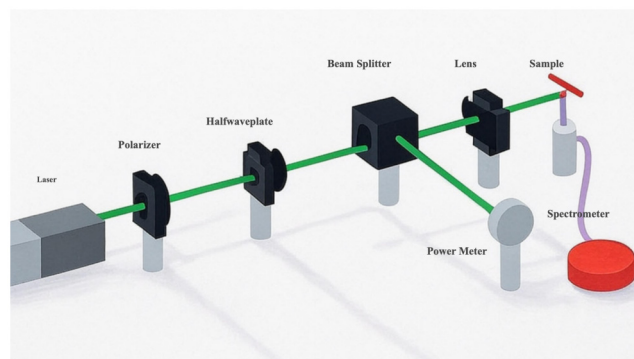


FIG. 1. Optical arrangement for random lasing.

energy to excite the PDCLC sample, and the other part is used as the reference light to record the pulse energy value with an energy meter. (According to the beam splitting ratio of the beam splitting prism and the reading of the energy meter, the corresponding pump energy can be given.) Due to the size of the pump spot, a cylindrical lens ( $f = 20 \text{ cm}$ ) was used to focus it in the experiment, and the sample was placed at the lens's focal point. Under the action of the pump light source, the emitted random laser is collected by the high-resolution spectrometer (HR4000 fiber spectrometer with a working spectrum width of 550–660 nm and a resolution of 0.04 nm), and the spectral details of the random laser are characterized. In this way, the characteristics of the random laser are studied as they change with the pump pulse laser. In the experimental results, the random laser we detected was emitted along the capillary's axial direction. This is because, due to the limitation of the inner diameter of the capillary, the intensity of the random laser emitted in the axial direction is relatively large and easy to detect. Random lasers with any emission angle can also be detected. A random laser can be detected in any direction, including the capillary wall.

## A. Materials and sample preparation

The polymer-dispersed chiral liquid crystal (PDCLC) mixture consists of dipentaerythritol pentaacrylate (DPHPA, 29 wt. %), the co-polymer cross-linking agent *n*-vinyl-2-pyrrolidone (NVP, 10 wt. %), the co-initiator *n*-phenylglycine (NPG, 0.8 wt. %), the photoinitiator rose bengal (RB, 0.1 wt. %), the laser dye 4-(dicyanomethylene)-2-methyl-6-(4-dimethylamino-styryl)-4H-pyran (DCM, 0.1 wt. %), the nematic liquid crystal E7 (31 wt. %, supplied by Merck), phthalate diglycol diacrylate (PDDA, 29 wt. %, supplied by Western Asia Company), and the chiral dopant S811 (17 wt. %). The MNPs, supplied by Dona Company, were modified with oleic acid and had a nominal diameter of 10 nm. The nanoparticles were dispersed into the LC using ultrasonic agitation to ensure a uniform distribution. The concentration of MNPs was varied across five different levels: 0, 0.01, 0.02, 0.03, and 0.04 wt. %. Once the nanoparticles were properly dispersed, the PDCLC samples were loaded into capillary tubes, which served as the optical cavities for the random lasing

06 December 2025 08:36:25

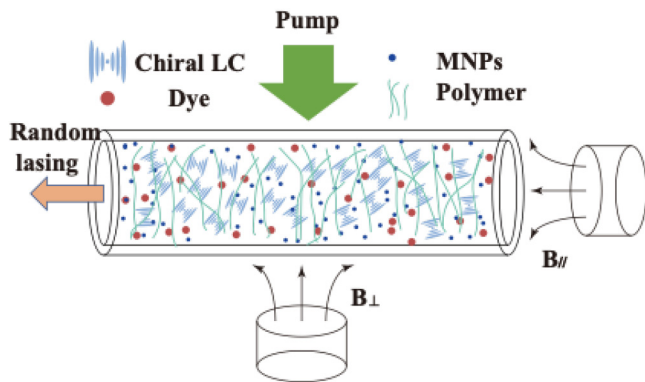


**FIG. 2.** Schematic diagram illustrating the excitation of random lasing from a PDCLC-filled capillary under magnetic fields applied in different directions.

measurements. After sealing the capillary tubes, the samples were cured under ultraviolet (UV) light to solidify the polymer matrix, maintaining the LC's alignment properties. Following this, the samples were subjected to external magnetic fields to modulate the orientation of the LC molecules and manipulate their optical properties.

The magnet used as the source of the magnetic field was in the form of a cylindrical NdFeB magnet, as it has relatively high magnetic-field strength. The strength of the magnetic field allowed the distance between the magnet and the capillary, where the sample was contained, to be altered. To determine directional effects, it was ensured that the cylindrical magnet was located in both axial ( $B$  parallel or  $B_{\parallel}$ ) and transverse ( $B$  perpendicular or  $B_{\perp}$ ) directions, as shown schematically in Fig. 2.

The energy of the pumping light was adjusted to a range of six levels: 7, 8, 10, 12, 15, and  $18 \mu\text{J}/\text{pulse}$ . The strength of the applied magnetic field over parallel and perpendicular orientations was 0, 2, 6, 8, and 10 mT.

## B. Characterization techniques

The uniformity of the LC alignment and nanoparticle dispersion in PDCLC samples was ensured using Polarized Optical Microscopy (POM). This methodology enabled us to verify the orientation of the LC molecules and verify the phase separation between the polymer and the LC phase of the film. Moreover, the morphology and size of MNPs in the samples were observed using Scanning Electron Microscopy (SEM). The SEM provided detailed images of the nanoparticles, confirming their dispersion and enabling evaluation of how size and distribution can affect the scattering properties of the PDCLC. In Fig. 3(a), photos of samples with various MNP concentrations are shown, from left to right: 0.01, 0.02, 0.03, and 0.04 wt. %. As shown in Fig. 3, the color becomes more saturated at high MNP concentrations due to increased light absorption. Figure 3(b) shows the sample images under polarized optical microscopy. It can be seen that the light was scattered uniformly, indicating that phase separation was complete. The radius of the MNPs is approximately 10 nm, as shown in Fig. 3(c), consistent with the vendor's data.

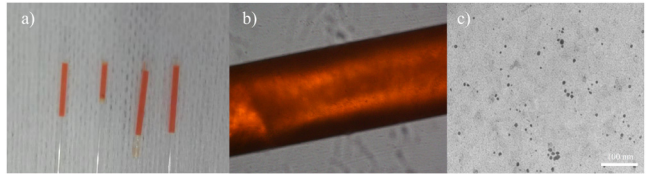


**FIG. 3.** (a) Photo of samples with various MNP concentrations (from left to right: 0.01, 0.02, 0.03, and 0.04 wt. %). (b) POM image of samples. (c) Ferromagnetic nanoparticles under a scanning electron microscope (scale bar: 100 nm).

## C. Machine learning approach

### 1. Data collection, description, and pre-processing

To predict and analyze random lasing behavior and its dependence on experimental parameters, machine-learning models were trained on a dataset combining both experimental and derived data. The dataset comprised 270 samples, including key parameters, such as magnetic nanoparticle (MNP) concentration (ranging from 0 to 0.04 wt. %), magnetic field strength (0, 2, 6, 8, and 10 mT), pumped energy levels (7, 8, 10, 12, 15, and  $18 \mu\text{J}/\text{pulse}$ ), and magnetic-field direction ( $B_{\parallel}$ ,  $B_{\perp}$ ). Emission-intensity values for each parameter combination were incorporated as target outputs. Regression models, such as random forests and Support Vector Machines (SVMs), were applied to predict lasing intensity based on these parameters.

06 December 2025 08:36:25

### 2. Overview of models

1. *Artificial neural network (ANN)*. ANNs mimic the synaptic processing of the human brain by interconnecting simple computational units called neurons.<sup>16</sup> Each neuron receives input signals, applies an activation function, and transmits the output through weighted connections. Thus, the performance of an ANN depends on its architecture, weight values, and activation functions. As shown in Fig. 4, a neuron receives inputs  $x_i$  ( $i = 1, 2, \dots, n$ ), each associated with a weight  $w_i$ . It computes a weighted sum and applies an activation function  $\phi$ , yielding the output

$$y = \phi \left( \sum_{i=1}^n w_i x_i + b \right). \quad (1)$$

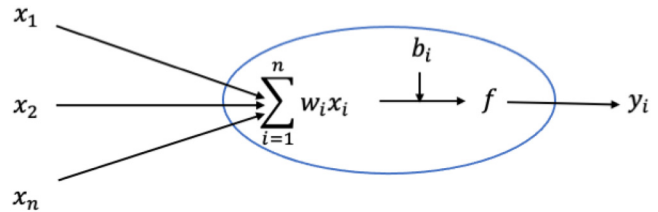


**FIG. 4.** A schematic of an artificial neuron process.

Here,  $b$  is a bias term that adjusts the activation threshold, and  $\phi$  introduces nonlinearity, allowing the network to capture complex patterns. A commonly used activation function is the sigmoid

$$f(x) = \frac{1}{1 + e^{-x}}. \quad (2)$$

**2. Support vector machine (SVM).** SVMs are supervised learning models for classification and regression that construct an optimal hyperplane maximizing the margin between classes.<sup>17</sup> The closest data points, called *support vectors*, define this boundary, making the model sparse and efficient. For regression, Support Vector Regression (SVR) fits a function within a tolerance margin. Nonlinear problems are handled using kernel functions, such as the Gaussian (RBF) kernel,

$$K(x, x') = \exp\left(-\frac{\|x - x'\|^2}{2\sigma^2}\right). \quad (3)$$

The *kernel trick* enables SVMs to capture complex relationships without explicit transformations.

**3. Random forest (RF).** Random Forest (RF) is an ensemble learning algorithm based on bagging, where multiple decision trees are trained on bootstrap samples and combined to produce robust predictions.<sup>18</sup> At each node split, a random subset of features is considered, reducing correlation between trees and improving generalization. For classification, predictions are made by a majority vote and for regression, by averaging tree outputs. A key strength of RF is its built-in validation using Out-of-Bag (OOB) samples (37% of data not used in tree training). An OOB error provides an unbiased estimate of generalization, while permutation of feature values in OOB samples measures variable importance. RF effectively captures nonlinear patterns and mitigates overfitting compared to single decision trees.

**4. XGBoost (extreme gradient boosting).** XGBoost is a scalable and efficient implementation of gradient boosting, widely used for supervised learning due to its strong predictive performance.<sup>19</sup> Unlike random forest, which builds independent trees in parallel, XGBoost constructs trees sequentially, with each tree correcting errors of the previous ensemble by fitting the negative gradient of the loss function. This iterative boosting process reduces bias and improves accuracy.

Its advantages include built-in L1/L2 regularization to prevent overfitting, optimized handling of sparse or missing data, and high computational efficiency through parallel processing and pruning. Like random forest, XGBoost also provides feature importance measures based on split frequency and contribution to loss reduction. In this research, XGBoost is applied for regression, leveraging its ability to model complex nonlinear relationships while maintaining robustness and scalability.

### 3. Machine-learning model development process

Data-driven machine-learning models for predicting random lasing intensity undergo several steps, as illustrated in Fig. 5.

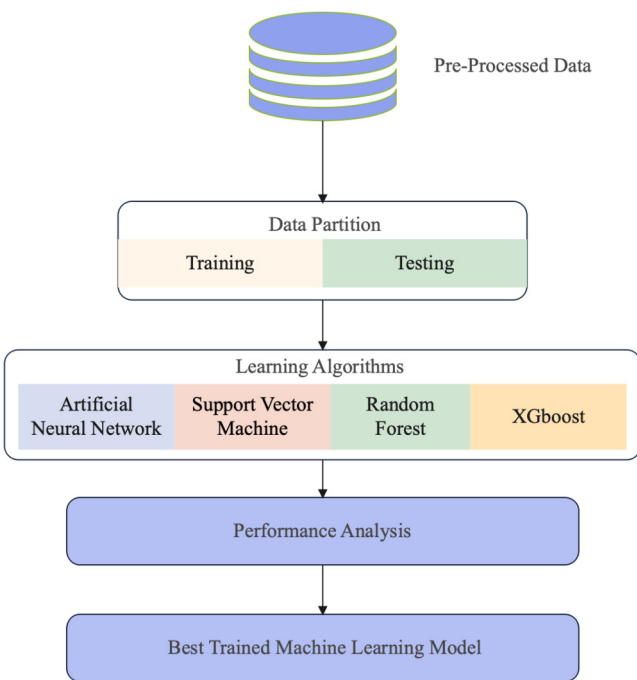


**FIG. 5.** Workflow diagram illustrating the machine-learning model development process.

06 December 2025 08:36:25

The input and output data are preprocessed and split into training and test subsets. The chosen machine-learning algorithms are then trained on the training set, and their performance is measured on the testing set. Lastly, the most effective model is selected to make a precise prediction of the random lasing properties.

The dataset was split into training and test sets, with 80% used for training and 20% for testing. This 80/20 divide is not universal but is rather agreed upon universally and provides a balance between learning and evaluation. The regression algorithms were used to create predictive models that estimated continuous outputs, with random laser intensity as the variable of interest. Managing machine-learning models can be quite sensitive because hyperparameters heavily determine performance; therefore, careful tuning is necessary. The grid search method was used to find the best hyperparameter values for each regression model systematically. Table I summarizes the chosen parameters.

To ensure reproducibility, the random number generator was initialized with a fixed seed. All models were implemented in Python (v3.10) on a 2.5 GHz Quad-Core Intel Core i7 system with 16 GB RAM. Model performance was assessed using two standard statistical metrics: the coefficient of determination ( $R^2$ ) and the root mean squared error (RMSE).

$R^2$  measures the goodness of fit and is defined as

$$R^2 = 1 - \frac{\sum_{t=1}^N (y_t - \hat{y}_t)^2}{N \cdot \text{var}(y)}, \quad (4)$$

**TABLE I.** Summary of machine-learning models and their configurations.

Model	Configuration
ANN	1 hidden layer (10 neurons); tangent sigmoid output function; Levenberg–Marquardt training; mean square error; initial gain 0.001; gain decrease 0.1; gain increase 10; max gain $1 \times 10^{10}$ ; minimum gradient $1 \times 10^{-7}$ ; maximum epochs 1000
SVM	RBF kernel (scale = 3.7); $C = 0.741$ ; $\varepsilon = 0.074$ ; optimized via SMO
RF	100 regression trees; random feature selection ( $mtry = \sqrt{p}$ ); bagging ensemble; random state = 42
XGBoost	100 regression trees; MSE loss; learning rate = 0.3; max depth = 6; L1 regularization ( $\alpha = 0$ ); L2 regularization ( $\lambda = 1$ ); subsampling ratio = 1.0; random state = 42

where  $\hat{y}_t$  and  $y_t$  represent the predicted and actual values at sample  $t$ , respectively, and  $N$  denotes the total number of samples in the dataset. The  $R^2$  value indicates how well the model replicates the observed outcomes, ranging from 0 to 1. An  $R^2$  of 1 implies perfect prediction accuracy, while an  $R^2$  of 0 indicates no predictive capability.

The RMSE quantifies the average magnitude of prediction errors and is calculated as the square root of the mean squared difference between predicted and actual values,

$$\text{RMSE} = \sqrt{\frac{1}{N} \sum_{t=1}^N (\hat{y}_t - y_t)^2}. \quad (5)$$

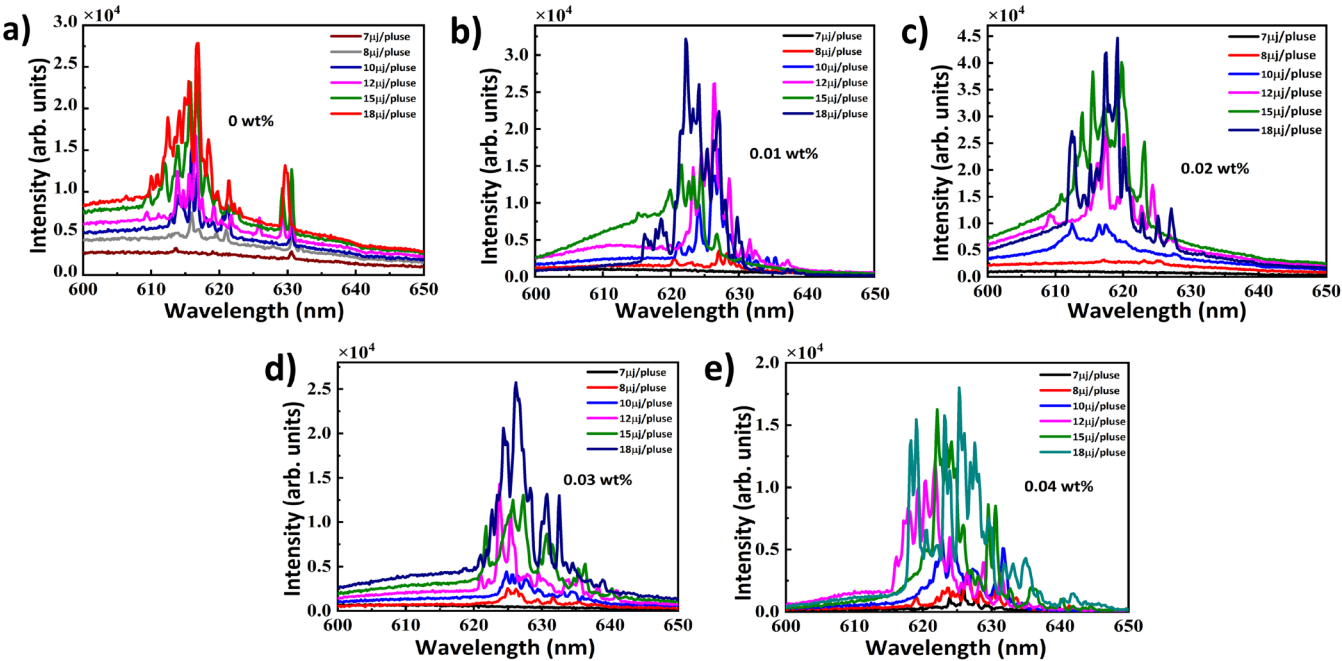


**FIG. 6.** Random lasing spectra with various concentrations from (a) to (e).

### III. RESULTS

This section first discusses experimental results and then machine-learning results.

#### A. Experimental results

The random lasing properties at various MNP concentrations are illustrated in Fig. 6. The lasing threshold varied with MNP concentration; however, no clear trend emerged. For instance, the threshold for PDCLC without MNPs was similar to that of samples with 0.01, 0.02, and 0.03 wt. % MNPs, but decreased at 0.04 wt. %, likely due to the enhanced scattering from the MNPs. The emission intensity increased as the MNP concentration rises from 0 to 0.02 wt. %, peaking at 0.02 wt. %, before decreasing as the concentration increased further. This behavior can be attributed to the enhanced scattering at higher MNP concentrations, which initially improves random lasing emission but eventually reduces output intensity as scattering becomes too strong.

The envelope of the random emission was analyzed, as shown in Fig. 6. A slight shift in emission wavelengths was observed with varying MNP concentrations. For undoped PDCLC, the random emission range was 610–630 nm, while for doped samples, the lasing emission ranges were 620–630 (0.01), 610–630 (0.02), 620–640 (0.03), and 615–640 nm (0.04 wt. %), respectively. The emission range for 0 and 0.02 wt. % MNPs was similar, likely due to the balance between enhanced scattering and improved random lasing. Initially, scattering boosts random lasing but weakens its directional output. At 0.02 wt. %, this balance maximized the emission intensity.

06 December 2025 08:36:25

As the MNP concentration increased further, stronger scattering formed multiple microcavities, leading to a more uniform distribution of random lasing peaks, as observed in the 0.04 wt. % sample in Fig. 6(e).

In our PDCLC composites, the CLC domains primarily serve as scattering centers, providing the multiple-scattering feedback essential for random lasing. For Bragg reflection to occur in a CLC, a well-aligned periodic structure is required; however, in PDCLC microdomains, the alignment between the polymer network and the CLC is random, preventing the formation of an ordered structure. Consequently, light is scattered by the CLC microdomains rather than undergoing Bragg reflection. The chiral dye further distorts the local director orientation, enhancing light scattering. Based on the refractive index and pitch of the CLC, the estimated photonic bandgap lies in the 500–600 nm range, whereas the observed lasing emission appears between 610 and 650 nm, well outside the stop band. This confirms that the lasing behavior in the PDCLC system is primarily governed by multiple scattering within polymer-dispersed CLC domains, with the scattering efficiency modulated by the magnetic field and MNP doping.

Next, the axial magnetic effect on random lasing in PDCLC with various MNP concentrations is illustrated in Fig. 7. The pumping energy was fixed at  $12\mu\text{J}/\text{pulse}$ , and the magnetic field was varied by adjusting the distance between the MNP and the PDCLC. As shown in Fig. 7(a), the emission intensity from undoped PDCLC decreased with an increasing magnetic field, reaching a maximum at 2 mT. This is due to the reorientation of LC molecules in response to an external magnetic field. Initially,

the LC molecules, randomly oriented due to unpolarized UV light, aligned in response to the magnetic field, enhancing scattering and random lasing. However, as the magnetic field increased, the LC molecules became fully aligned, reducing scattering and weakening random lasing. This trend is also observed in Figs. 7(b)–7(d) for MNP-doped samples (0.01–0.03 wt. %), where the magnetic effect on random lasing was similar to that of the undoped sample. This may be due to the fixed MNPs in the polymer matrix, which cannot respond to the magnetic field, while MNPs in the LC phase disturb the LC alignment, reducing scattering and weakening random lasing emission. Therefore, the magnetic effect on MNP-doped PDCLC had a negative impact on random lasing.

At sufficiently high MNP concentrations, the magnetic field had little effect on random lasing. As shown in Fig. 8(b), the emission intensity increases significantly when 10 mT magnetic field is applied, especially when compared to Fig. 8(a). The doping mechanism can explain this. At high concentrations, the scattering becomes intense, and the applied magnetic field induces alignment of the MNPs. The local concentration of MNPs increases, thereby enhancing random lasing emission.

We also investigated the impact of a transverse magnetic field on random lasing in PDCLC within a capillary, using a pump energy of  $12\mu\text{J}/\text{pulse}$ . As shown in Fig. 9, similar to the parallel magnetic field ( $B_{||}$ ), the transverse magnetic field ( $B_{\perp}$ ) reduced the random lasing emission. The 0.02 wt. % sample exhibited the highest intensity, while the 0.04 wt. % sample had the lowest threshold but weaker emission intensity. The random lasing emission decreased rapidly with increasing magnetic field strength, particularly for  $B_{\perp}$ , as the

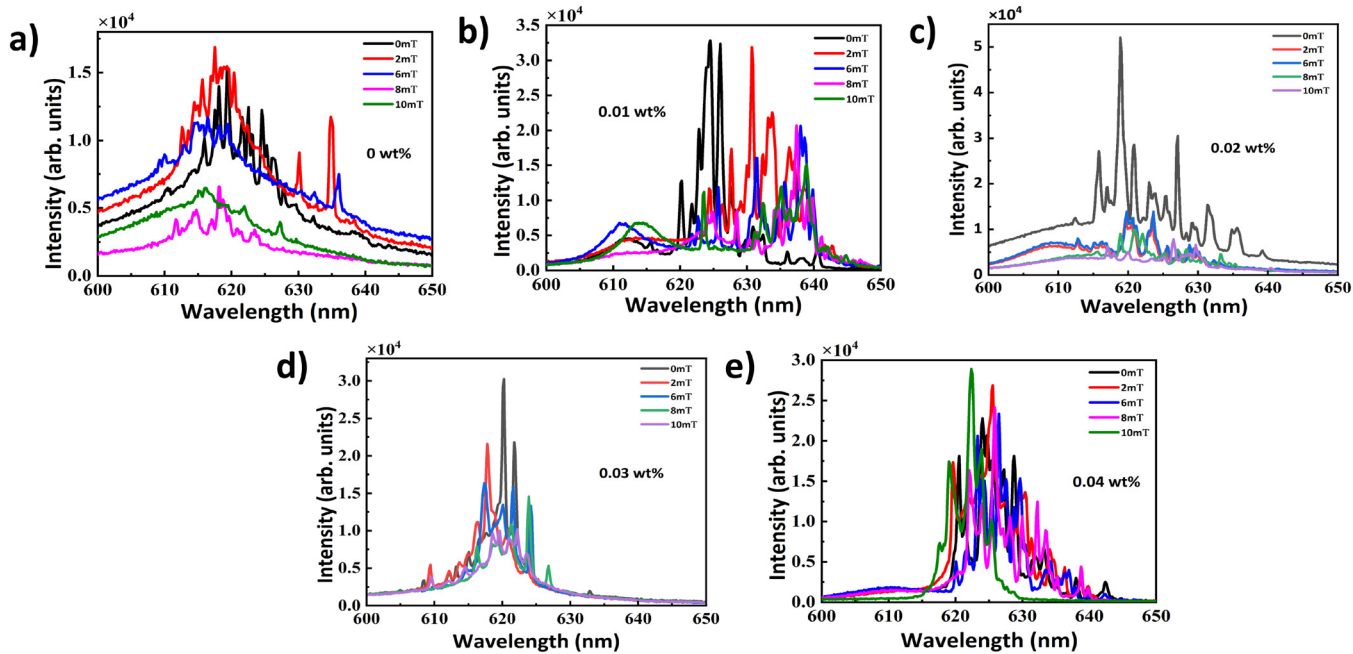


**FIG. 7.** Random lasing spectra under varying axial magnetic fields ( $B_{||}$ ) at a pump energy of  $12\mu\text{J}/\text{pulse}$  for PDCLC samples with (a) 0 wt. % undoped PDCLC, (b) 0.01 wt. %, (c) 0.02 wt. %, (d) 0.03 wt. %, and (e) 0.04 wt. % MNP-doped PDCLC.

06 December 2025 08:36:25

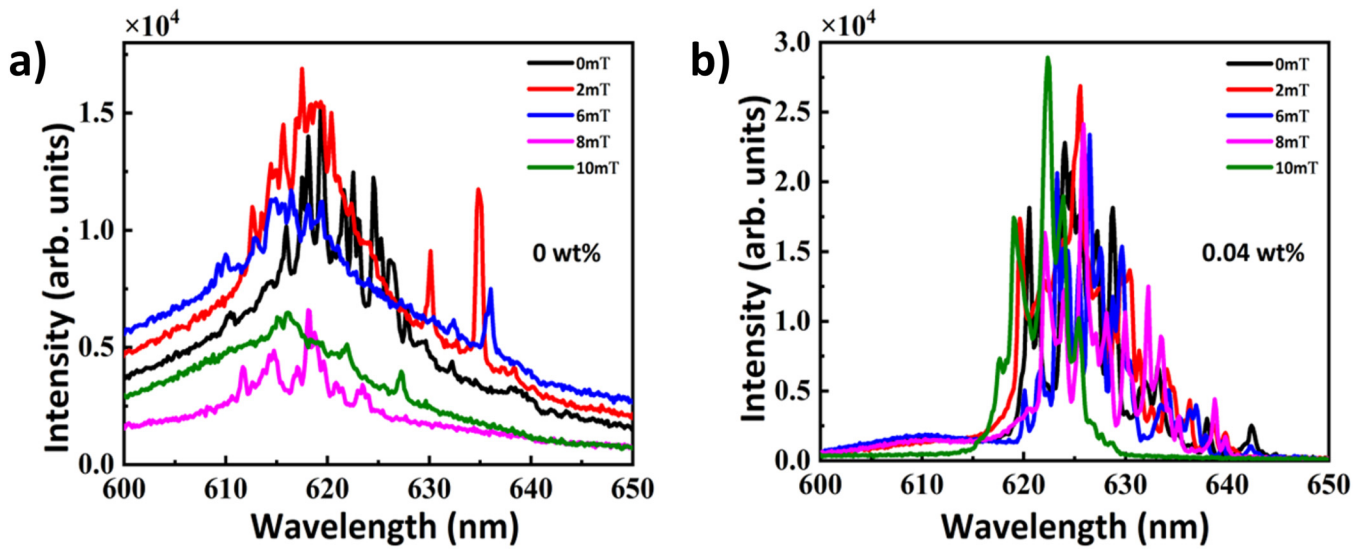


**FIG. 8.** Random lasing spectra under an axial magnetic field ( $B_{\parallel}$ ) at a pump energy of  $12 \mu\text{J}/\text{pulse}$  for PDCLC samples with (a) 0 wt. % undoped PDCLC and (b) 0.04 wt. % heavily-doped PDCLC.

magnet was positioned closer to the pumping location. The stronger suppression under transverse ( $B_{\perp}$ ) fields likely arises from enhanced local field distortions and reduced scattering anisotropy near the pump line. In this geometry, LC directors align perpendicular to the

propagation axis, reducing multiple scattering along the capillary and thereby weakening feedback. This anisotropic alignment diminishes the number of effective scattering centers contributing to feedback, explaining the sharper intensity drop under  $B_{\perp}$  compared to  $B_{\parallel}$ .

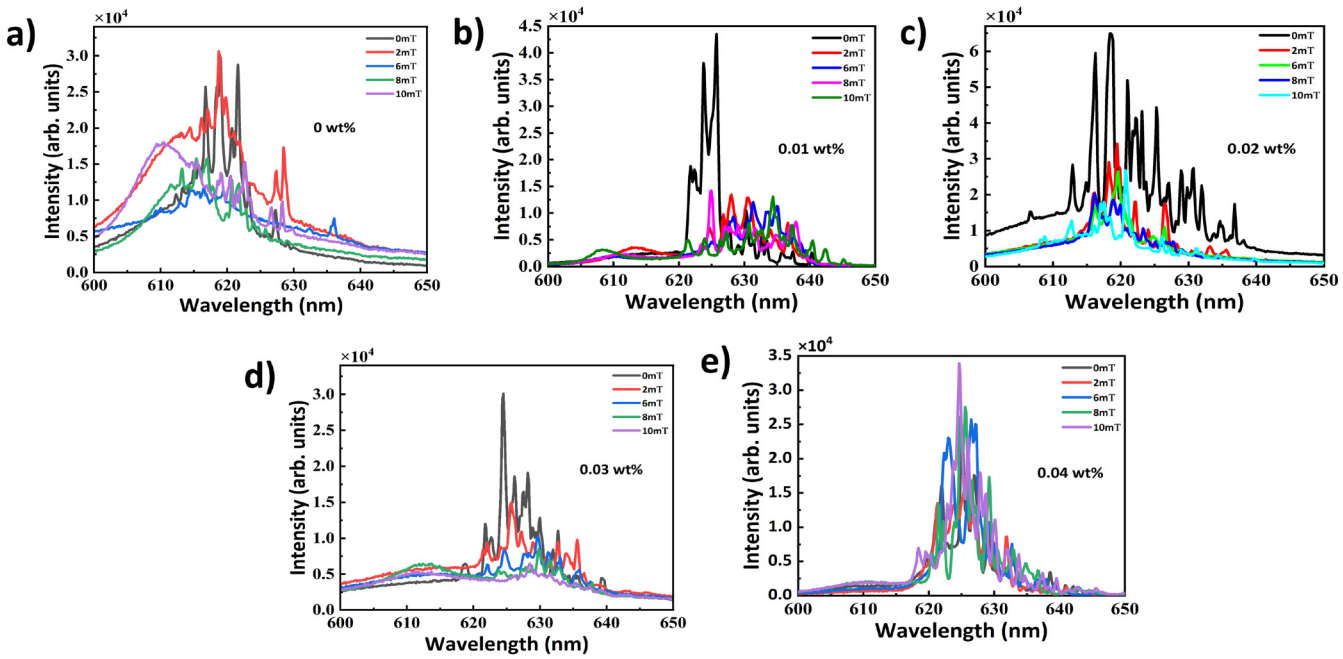


**FIG. 9.** Random lasing spectra under varying transverse magnetic field ( $B_{\perp}$ ) at a pump energy of  $12 \mu\text{J}/\text{pulse}$  for PDCLC samples with (a) 0 wt. % undoped PDCLC, (b) 0.01 wt. %, (c) 0.02 wt. %, (d) 0.03 wt. %, and (e) 0.04 wt. % MNP-doped PDCLC.

In our setup, the pump light was focused into a line using a cylindrical lens, which increased the field strength near the capillary surface. The magnetic field was weaker for  $B_{\parallel}$  as the magnet was placed at one end of the capillary. In the case of the 0.04 wt. % sample, strong scattering from the high MNP concentration diminished the magnetic effect. This is evident from the spectral profiles in Fig. 9, where the 0.04 wt. % sample exhibits a flat spectrum with random lasing peaks. In contrast, the undoped sample displays a Gaussian-like profile, indicating that most of the pump energy was converted into spontaneous emission rather than lasing.

### 1. Machine learning model performance

To evaluate the predictive capability of machine-learning models for lasing intensity in random lasing systems, four regression methods were employed: SVM, ANN, random forest, and XGBoost. These models were selected for their ability to capture nonlinear relationships in high-dimensional datasets, a characteristic inherent to random lasing behavior. The data were divided into training (80%) and test (20%) sets to evaluate generalization. The coefficient of determination ( $R^2$ ) and the root mean squared error (RMSE) were used to assess the performance of a model, and their results were summarized in Table II.

*1. Training performance.* The training set showed that all four models had exceptional predictive performance, with  $R^2$  values exceeding 0.93. XGBoost's performance was almost perfect ( $R^2 = 0.9999$ , RMSE = 3.25), indicating the model effectively captured intricate nonlinear relationships within the data. Random forest also demonstrated excellent training accuracy ( $R^2 = 0.9896$ , RMSE = 43.46), followed by ANN ( $R^2 = 0.9724$ , RMSE = 70.56) and SVM ( $R^2 = 0.9379$ , RMSE = 105.99).

*2. Testing performance.* On the independent test set, every model deployed achieved high predictive accuracy, attaining  $R^2$  values over 0.91. XGBoost achieved the best generalization, attaining an  $R^2$  of 0.9752 and an RMSE of 70.89, demonstrating solid performance on unseen data. Random forest demonstrates consistent performance on the training set and generalizes well ( $R^2 = 0.9416$ , RMSE = 108.83). ANN ( $R^2 = 0.9298$ , RMSE = 119.87) and SVM ( $R^2 = 0.9150$ , RMSE = 131.26) showed slightly weaker generalization, though still within acceptable limits.

Overall, XGBoost provided the closest approximation to the ideal generalized model, achieving near-perfect training accuracy while demonstrating robust generalization. Moreover, Random forest presented the most consistent performance throughout both

phases. Although ANN and SVM delivered relatively strong performances, they were outmatched by the ensemble-based models.

In Fig. 10, the predicted performance of the machine-learning models, SVM, ANN, random forest, and XGBoost, is illustrated by plotting predicted intensity vs actual intensity. The red-dashed line represents the ideal fit, and the blue dots are the model predictions. XGBoost shows the tightest clustering around the ideal fit and indicates the greatest consistency in predicted values. Random forest shows a moderately wider range of values but maintains proximity to the ideal fit, demonstrating stable performance in predictions. In contrast, ANN and SVM exhibit a greater deviation from the ideal fit and more dispersed patterns, resulting in lower prediction accuracy. These visuals capture the relative effectiveness of each model in describing the underlying relationships in the data.

Feature importance analysis for the XGBoost model is shown in Fig. 11. Here, the impact of key parameters that influence random lasing behavior is shown. The graphical representation indicates that "Magnetic field strength" is the predominant parameter, as it has the tallest bar, indicating its importance in the model's predictions. The importance of "Concentration" comes in second, although it is considerably lesser in importance than that of the strength of the magnetic field. The next most impactful parameter is "Pump energy." In contrast, "Magnetic field perpendicular" and "Magnetic field parallel" have the least importance. This is evidenced by their significantly shorter bars, which indicate that these two parameters have little influence on the predictive outcome. This illustration clearly shows how each feature affects the model differently and identifies which strengths and concentrations of the magnetic fields are the foremost contributors to the XGBoost model's performance.

06 December 2025 08:36:25

### 2. Comparative insights

XGBoost's outstanding performance is linked to its gradient boosting framework, which reduces prediction errors through iterative tree construction while effectively modeling complex nonlinear relationships. Due to the complexity of random lasing datasets, this ensemble approach employs regularization to control overfitting, and it effectively prevents overfitting. Random forest also employs averaging across multiple decision trees, producing robust, stable predictions while assigning importance values to each feature. However, XGBoost slightly outpaced it in both accuracy and generalization. In contrast, the ANN's flexibility in modeling nonlinear relationships was evident; however, its higher RMSE on the test set suggests potential sensitivity to hyperparameter choices or the need for more sophisticated architectures to avoid local minima during training. Although SVM is generally suitable for nonlinear mappings through kernel tricks, it appears to lack sensitivity to hyperparameters. It could be improved with more advanced tuning techniques, such as grid search optimization. The ensemble approach (XGBoost classifier and random forest) performed better than the others, which proves the advantages of aggregation when cleaning noisy, multifaceted physical data.

While our machine-learning models effectively captured the nonlinear dynamics of random lasing in  $\text{Fe}_3\text{O}_4$ -doped PDCLCs, achieving a test set  $R^2$  of 0.9752 with XGBoost, they are prone to overfitting. Despite employing regularization (e.g., L1/L2 in

TABLE II. Performance metrics of machine-learning models.

Model	Training		Testing	
	$R^2$	RMSE	$R^2$	RMSE
SVM	0.9379	105.99	0.9150	131.26
ANN	0.9724	70.56	0.9298	119.87
Random forest	0.9896	43.46	0.9416	108.83
XGBoost	0.9999	3.25	0.9752	70.89

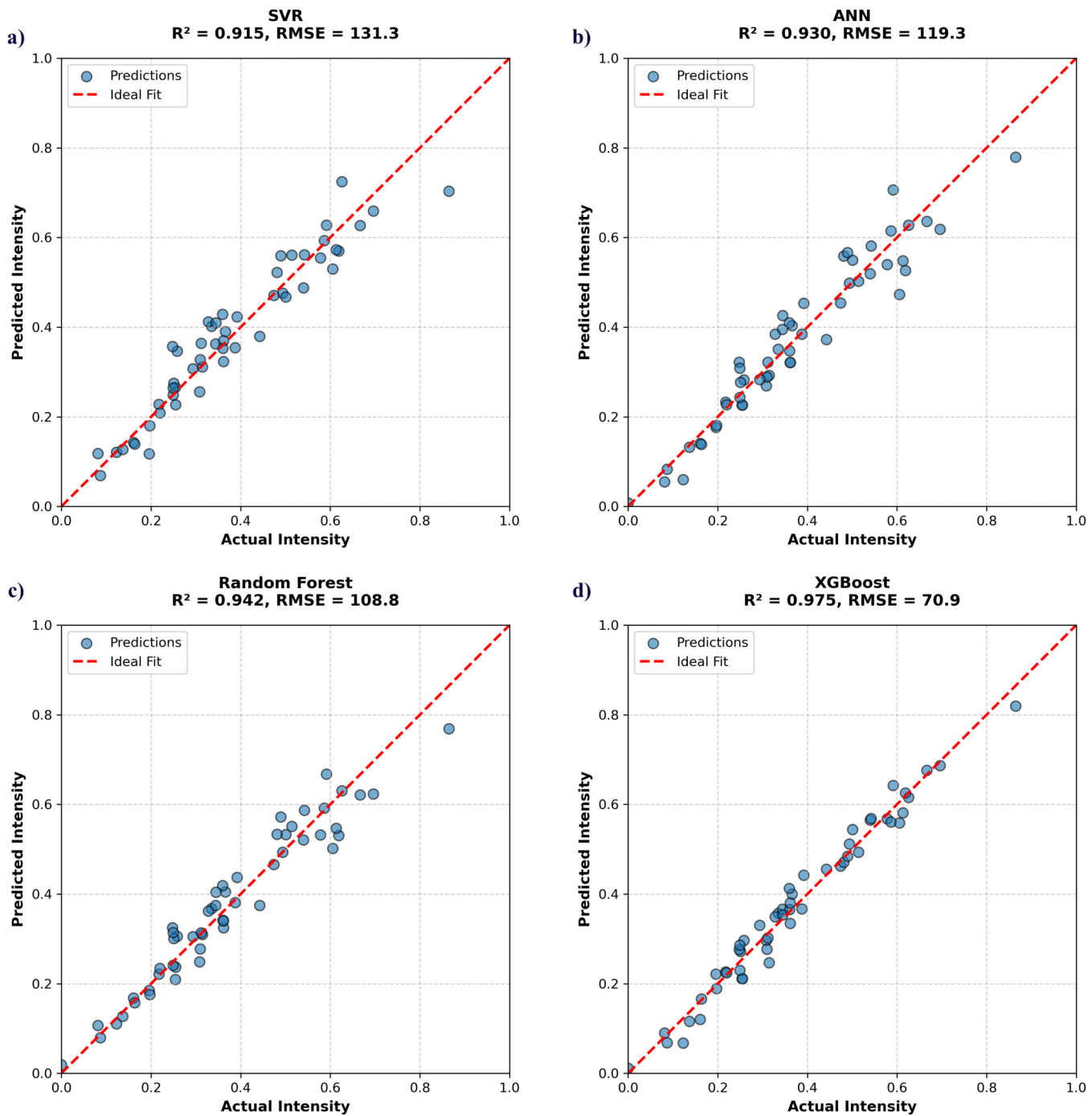


**FIG. 10.** Scatterplots illustrating the predicted vs actual intensity values for the four machine-learning models: (a) SVR, (b) ANN, (c) random forest, and (d) XGBoost.

06 December 2025 08:36:25

XGBoost) and an 80/20 train-test split, the relatively small dataset of 270 samples, coupled with the system's high-dimensional complexity, may exacerbate overfitting risks. Hyperparameter tuning via grid search mitigated some risks, but minor experimental noise or

fluctuations could still skew the fitted relationships, necessitating larger, more diverse datasets for greater stability. Moreover, the models' external validity is limited to the specific capillary-based PDCLC system with  $\text{Fe}_3\text{O}_4$  MNPs, and their applicability to other

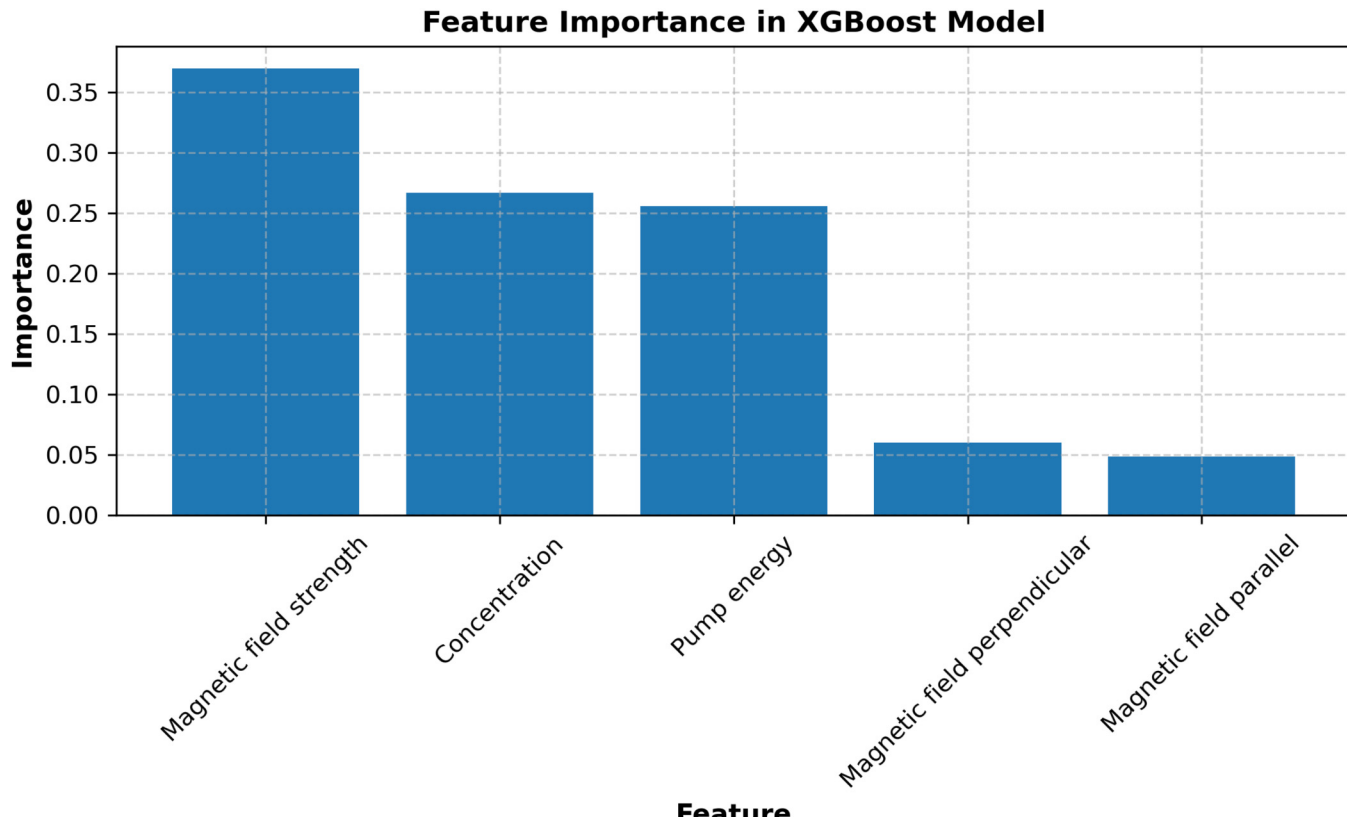


FIG. 11. Plot of feature importance in the XGBoost model.

06 December 2025 08:36:25

liquid crystal systems (e.g., different nematic hosts or chiral dopants) remains unverified. Future research should test these models against larger, independent datasets to demonstrate their reliability and generalizability across different photonic materials and contexts.

#### IV. IMPLICATIONS AND FUTURE WORK

Even in random lasing systems, these models maintain a high degree of accuracy, proving their applicability for real-time lasing intensity prediction within experimental scope. This significantly streamlines the subsequent design and photonic device optimization processes, reducing the time and effort spent on trial-and-error iterative improvements. Integrating these models into a simulation framework will enable researchers to anticipate laser behavior across different parameter settings, minimizing the duration of empirical investigations and accelerating advances in the use of lasers in communications and sensing technologies. Including other variables, such as environmental conditions (temperature and humidity) or more sophisticated material characteristics (nanoparticle distributions), will allow for greater model generalizability and the uncovering of more hidden relationships. Furthermore, investigating hybrid frameworks, including combining XGBoost with deep learning elements, such as recurrent neural networks for temporal integration,

or leveraging explainable artificial intelligence methods to improve explainability is likely to improve predictive efficacy. Finally, forthcoming research might employ reinforcement learning models to empower real-time feedback control of adaptive optimization of lasing performance by automatically varying magnetic field strength or pump settings.

#### V. CONCLUSION

In this work, the tunable random lasing characteristics of polymer-dispersed chiral liquid crystals (PDCLCs) doped with ferromagnetic nanoparticles (MNPs) have been investigated. The performed experiment indicates that both the intensity of the random lasing phenomenon and its spectral characteristics depend significantly on the concentration of MNPs and the application of a magnetic field. The lasing intensity depends non-monotonically on the MNP concentration, and an optimal concentration (0.02 wt. %) can be identified that maximizes the emission intensity. We also observed a blue shift in the emission spectrum under a magnetic field, with the magnitude differing between the axial and transverse directions. To gain deeper insight into how the system will behave, we trained a machine-learning model on a dataset generated from experimental data. The machine-learning models effectively

identified the main factors that affect intensity, facilitating an understanding of the ideal conditions for improving random lasing efficiency in PDCLC systems. This approach offers a promising approach to enhance the optimization of PDCLC-based random lasers, particularly for tunable optoelectronic devices.

This study illustrates the value of integrating empirical research with machine learning to enhance understanding of the mechanisms underlying random lasing in PDCLC systems. Future studies may extend this research by including additional predictors and refining machine-learning models to improve predictive precision. Magnetic-field modulation combined with machine learning paves the way for next-generation tunable random lasers with superior performance and versatility.

## ACKNOWLEDGMENTS

This work was supported, in part, by the National Natural Science Foundation of China (No. 62375200).

## AUTHOR DECLARATIONS

### Conflict of Interest

The authors have no conflicts to disclose.

### Author Contributions

**Aneela Ahmad:** Conceptualization (equal); Data curation (equal); Formal analysis (equal); Funding acquisition (equal); Investigation (equal); Methodology (equal); Resources (equal); Software (equal); Supervision (equal). **Haitao Dai:** Conceptualization (equal); Funding acquisition (equal); Supervision (equal). **Rafiqul Haq:** Data curation (equal); Methodology (equal); Writing – review & editing (equal). **Shouzhong Feng:** Data curation (equal); Funding acquisition (equal); Software (equal). **Aisha Rani:** Methodology (equal); Software (equal); Visualization (equal). **Buyi Yao:** Formal analysis (equal); Methodology (equal); Visualization (equal). **Yuhan Wang:** Data curation (equal); Methodology (equal).

## DATA AVAILABILITY

The data that support the findings of this study are available from the corresponding author upon reasonable request.

## REFERENCES

- <sup>1</sup>D. S. Wiersma, “The physics and applications of random lasers,” *Nat. Phys.* **4**, 359–367 (2008).
- <sup>2</sup>H. Zhou, H. Wang, W. He, Z. Yang, H. Cao, D. Wang, and Y. Li, “Research progress of cholesteric liquid crystals with broadband reflection,” *Molecules* **27**, 4427 (2022).
- <sup>3</sup>A. Ahmad, H. Dai, S. Feng, M. Li, D. Mehvish, Z. Mohmaed, S. Arain, Z. Chen *et al.*, “Recent advances in lasing phenomena in cholesteric liquid crystals: Materials, mechanisms and applications,” *Phys. Chem. Chem. Phys.* **27**, 15293 (2025).
- <sup>4</sup>R.-q. Tang, M.-l. Lu, R. Duan, and D.-y. Zhao, “Research progress of cellulose nanocrystal chiral liquid crystal film,” *Chin. J. Liq. Cryst. Disp.* **37**, 1263–1277 (2022).
- <sup>5</sup>R. Wu, R.-x. Shi, X. Wu, J. Wu, and Q. Dai, “Random lasing in dye-doped polymer dispersed liquid crystal film,” *Chin. Phys. B* **25**, 094209 (2016).
- <sup>6</sup>S. Mani, S. Mani, S. Khosla, and P. Sarawade, “Tuning of thermal and electrical properties of polymer dispersed cholesteric liquid crystal,” in *Materials Science Forum* (Trans Tech Publications, 2022), Vol. 1070, pp. 33–43.
- <sup>7</sup>H. Hu and Z. Zheng, “Progress on chiral photoswitches for constructing liquid crystal helical structures,” *Chin. J. Liq. Cryst. Disp.* **40**, 75–94 (2025).
- <sup>8</sup>C.-Y. Tsai, Y.-M. Liao, W.-C. Liao, W.-J. Lin, P. Perumal, H.-H. Hu, S.-Y. Lin, C.-H. Chang, S.-Y. Cai, T.-M. Sun *et al.*, “Magnetically controllable random lasers,” *Adv. Mater. Technol.* **2**, 1700170 (2017).
- <sup>9</sup>O. Gornitska, A. Koval’chuk, T. Koval’chuk, P. Kopčanský, M. Timko, V. Zavisova, M. Koneracka, N. Tomašovičová, J. Jadzyn, and I. Studenýak, “Dielectric properties of nematic liquid crystals with Fe<sub>3</sub>O<sub>4</sub> nanoparticles in direct magnetic field,” *Semicond. Phys. Quantum Electron. Optoelectron.* **12**, 309 (2009).
- <sup>10</sup>F. Ahmad, M. Lugman, and M. Jamil, “Advances in the metal nanoparticles (MNPs) doped liquid crystals and polymer dispersed liquid crystal (PDLC) composites and their applications—A review,” *Mol. Cryst. Liq. Cryst.* **731**, 1–33 (2021).
- <sup>11</sup>H. T. Dai, M. N. Gao, Y. X. Xue, A. X. Xiao, A. Ahmad, Z. Mohamed, C. L. Liu, Q. Lu, and S. Z. Feng, “Magnetically tunable random lasing from polymer dispersed liquid crystal doped ferromagnetic nanoparticles in capillary,” *AIP Adv.* **9**, 115015 (2019).
- <sup>12</sup>R.-n. Wu, X. Wang, F. Yang, Y.-q. Li, Q. Dai *et al.*, “Realization of random lasing in dye-doped chiral nematic liquid crystal,” *Chin. J. Liq. Cryst. Disp.* **33**, 464–468 (2018).
- <sup>13</sup>E. P. Santos, R. F. Silva, C. V. T. Maciel, D. F. Luz, and P. F. A. Silva, “Investigation of random laser in the machine learning approach,” *Braz. J. Phys.* **54**, 70 (2024).
- <sup>14</sup>G. Carleo, I. Cirac, K. Cranmer, L. Daudet, M. Schuld, N. Tishby, L. Vogt-Maranto, and L. Zdeborová, “Machine learning and the physical sciences,” *Rev. Mod. Phys.* **91**, 045002 (2019).
- <sup>15</sup>P. R. Wiecha, “Deep learning for nano-photonics—the solution to everything?” *Curr. Opin. Solid State Mater. Sci.* **28**, 101129 (2024).
- <sup>16</sup>D. E. Rumelhart, G. E. Hinton, and R. J. Williams, “Learning representations by back-propagating errors,” *Nature* **323**, 533–536 (1986).
- <sup>17</sup>V. Vapnik, *The Nature of Statistical Learning Theory* (Springer Science & Business Media, 2013).
- <sup>18</sup>L. Breiman, “Random forests,” *Mach. Learn.* **45**, 5–32 (2001).
- <sup>19</sup>T. Chen and C. Guestrin, “XGBoost: A scalable tree boosting system,” in *Proceedings of the 22nd ACM SIGKDD International Conference on Knowledge Discovery and Data Mining* (Association for Computing Machinery, 2016), pp. 785–794.